Measurement of red blood cell mechanics during morphological changes

YongKeun Park[a], Catherine A. Best[b], Kamran Badizadegan[a,c], Ramachandra R. Dasari[a], Michael S. Feld[a], Tatiana Kuriabova[d], Mark L. Henle[e], Alex J. Levine[f,1], and Gabriel Popescu[a,g,1]

[a]G. R. Harrison Spectroscopy Laboratory, Massachusetts Institute of Technology, Cambridge, MA 02139; [b]College of Medicine, University of Illinois at Urbana-Champaign, Urbana, IL 61801; [c]Department of Pathology, Harvard Medical School and Massachusetts General Hospital, Boston, MA 02114; [d]Department of Physics, University of Colorado, Boulder, CO 80309; [e]School of Engineering and Applied Sciences, Harvard University, Cambridge, MA 02138; [f]Department of Chemistry and Biochemistry, University of California, Los Angeles, CA 90095; and [g]Quantitative Light Imaging Laboratory, Department of Electrical and Computer Engineering, Beckman Institute for Advanced Science and Technology, University of Illinois at Urbana-Champaign, Urbana, IL 61801

Edited by Tom C. Lubensky, University of Pennsylvania, Philadelphia, PA, and approved February 26, 2010 (received for review August 23, 2009)

The human red blood cell (RBC) membrane, a fluid lipid bilayer tethered to an elastic 2D spectrin network, provides the principal control of the cell's morphology and mechanics. These properties, in turn, influence the ability of RBCs to transport oxygen in circulation. Current mechanical measurements of RBCs rely on external loads. Here we apply a noncontact optical interferometric technique to quantify the thermal fluctuations of RBC membranes with 3 nm accuracy over a broad range of spatial and temporal frequencies. Combining this technique with a new mathematical model describing RBC membrane undulations, we measure the mechanical changes of RBCs as they undergo a transition from the normal discoid shape to the abnormal echinocyte and spherical shapes. These measurements indicate that, coincident with this morphological transition, there is a significant increase in the membrane's shear, area, and bending moduli. This mechanical transition can alter cell circulation and impede oxygen delivery.

membrane dynamics | microrheology | quantitative phase imaging

Quantifying the mechanics of live red blood cells (RBCs) promises more sensitive probes of their structure at the nanoscale and suggests new insights into the etiology of a number of human diseases (1, 2). In the healthy individual, these cells withstand repeated, large-amplitude mechanical deformations as they circulate through the microvasculature. Certain pathological conditions such as spherocytosis, malaria, and Sickle cell disease cause changes in both the equilibrium shape and mechanics of RBCs, which impact their transport function. Here we communicate measurements of RBC mechanics that rely on unique experimental and theoretical techniques to characterize the mechanics/rheology of normal and pathological RBCs over a range of length and time scales.

Lacking a 3D cytoskeleton, RBCs maintain their shape and mechanical integrity through a spectrin-dominated, triangular 2D network attached to the cytosolic side of their plasma membrane. This semiflexible filament network, along with the surface tension of the bilayer, contributes to the elastic moduli of the composite membrane (3). The fluid lipid bilayer is thought to be the principal contributor to its bending or curvature modulus. Little is known about the molecular and structural transformations that take place in the membrane and spectrin network during the cell's morphological transitions from discocyte (DC, normal shape) to echinocyte (EC, spiculated shape) to spherocyte (SC, nearly spherical) (Figs. 1 *A–C*), which are accompanied by changes in RBC mechanics.

A number of techniques have been used to study the rheology of live cells (2). Micropipette aspiration (4), electric field deformation (5), and optical tweezers (2) provide quantitative information about the shear and bending moduli of RBC membranes in static conditions. However, dynamic, frequency-dependent knowledge of RBC mechanics is currently very limited with the notable exception of ref. 6. RBC thermal fluctuations ("flickering") have been studied for more than a century (7) to better understand the interaction between the lipid bilayer and the cytoskeleton (1, 8, 9). Nevertheless, quantifying these motions is experimentally challenging; reliable spatial and temporal data are desirable (1, 8, 10–13).

We use diffraction phase microscopy (DPM) (14, 15) to study the undulatory dynamics of RBC membranes over the commonly occurring DC-EC-SC shape transition. DPM is a highly sensitive imaging technique that provides quantitative, high-stability maps of the optical paths across living cells (Figs. 1 *A–C*). This optical pathlength information can be readily translated into cell thickness, since mature RBCs, lacking nuclei and other internal structures, have a spatially uniform refractive index. Using this technique, the flickering of RBC membranes can be measured with nanometer accuracy. From these measurements, we extract the frequency-dependent viscoelastic moduli of the composite RBC membrane.

We use a fluctuation-based approach to measure the cells' elastic properties. Using the equipartition theorem, the observed fluctuation amplitude at a point on the membrane, parametrized by the mean squared normal displacement $\langle \Delta h^2 \rangle$, determines in thermal equilibrium an *effective local spring constant* $k_e = k_B T / \langle \Delta h^2 \rangle$. This heuristic model incorrectly treats each patch of the membrane as an independent harmonic oscillator, so k_e will not be quantitatively accurate. However, it does give a qualitative measure of the spatial heterogeneity of the membrane within one cell and of the mechanical differences between cells. In the next section we develop a quantitative approach to the fluctuations, but to semiquantitatively characterize the data, we map the cells in terms of k_e (Figs. 2 *A–C*). The resulting k_e maps reveal fixed material inhomogeneities, particularly in ECs and SCs. For normal (DC) cells the central "dimple" appears to be stiffer (Fig. 2*A*). This feature of the spatial distribution of k_e may be due to local variations of both membrane curvature and the structural properties of the underlying spectrin network. When such spatial heterogeneities are averaged over, we find that SCs are characterized by an elastic constant 4 times larger than that of DCs (Fig. 2*D*). Over the morphological transition from DC to SC, $\sqrt{\langle \Delta h^2 \rangle}$ decreases progressively from 46 nm (DCs) to 34 nm (ECs) and 15 nm (SCs), indicating an increasing cell stiffness

Author contributions: Y.P., A.J.L., and G.P. designed research; Y.P. and C.A.B. performed research; C.A.B., K.B., R.R.D., M.S.F., and G.P. contributed new reagents/analytic tools; Y.P., T.K., M.H., A.J.L., and G.P. analyzed data; and Y.P., A.J.L., and G.P. wrote the paper.

The authors declare no conflict of interest.

This article is a PNAS Direct Submission.

Freely available online through the PNAS open access option.

[1]To whom correspondence may be addressed. E-mail: gpopescu@illinois.edu or alevine@chem.ucla.edu.

This article contains supporting information online at www.pnas.org/cgi/content/full/0909533107/DCSupplemental.

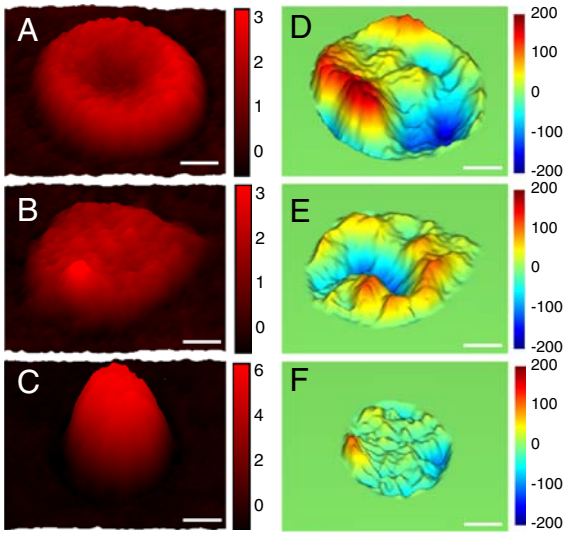

Fig. 1. Red blood cells in three different morphologies (*A*)–(*C*) and instant displacement map (*D*)–(*F*). (*A*) Typical RBC physical maps for DC, (*B*) EC, and (*C*) SC obtained by DPM (color bar represents thickness in *m*). (*D*)–(*F*) Respective instantaneous displacement maps (color bar in nm). Scale bar, 1.5 μm.

(Figs. 1 *D–F*). The average elastic constant measured for DCs, $k_e = 1.9$ μN/m, is a factor of 3.5–10 lower than what was measured by micropipette aspiration (16) and electric field deformation (5). However, the quantitative theory discussed below and used to analyze our data generates elastic constants for DCs in good agreement with previous work.

To quantitatively investigate the material properties of RBCs in various cellular morphologies, we analyze the undulatory membrane fluctuations by measuring the spatial and temporal correlations of the out-of-plane motions. We interpret these measurements using a unique viscoelastic continuum model of the composite spectrin-network/lipid membrane. This model accounts for the linear coupling between the bending and compression modes of a curved membrane, and thus provides a more accurate description of the dynamics of the RBC than theories based on a flat membrane.

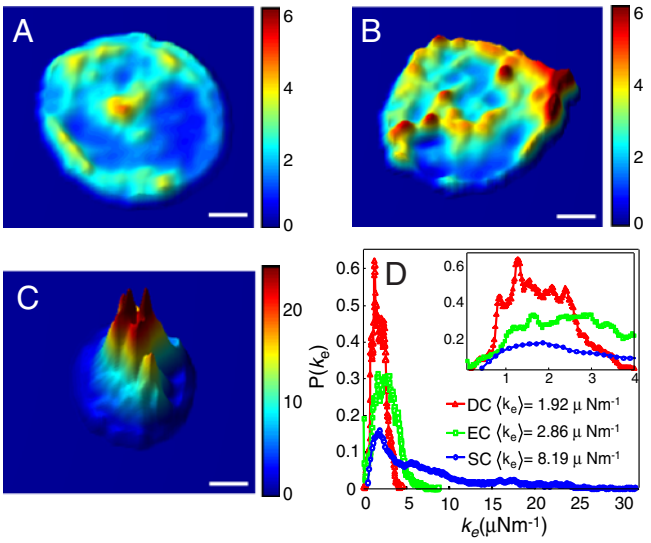

Fig. 2. The effective spring constant (k_e). (*A*)–(*C*) Typical effective spring constant map for DC (*A*), EC (*B*), and SC (*C*). Color bars are in μNm^{-1}; scale bar, 1.5 μm. (*D*) Corresponding histograms of the effective spring constant. The legend shows the respective mean values $\langle k_e \rangle$. The inset details the $\langle k_e \rangle$ behavior in the vicinity of the origin.

Analysis

The Fluctuation Spectrum of a Viscoelastic Shell. It was shown by Lennon and Brochard (1) that the decay rate of the undulations of a globally flat lipid bilayer in a viscous solvent scales as $\omega_q^{\mathrm{LB}} \sim q^3$, where q is the transverse wavenumber. This can be understood as resulting from a balance of a restoring force proportional to q^4, due to the bilayer's bending rigidity, and a q-dependent (i.e. nonlocal) hydrodynamic drag. Strikingly, this fundamental theory is unable to account for experimental measurements of the undulatory dynamics of RBCs; rather, decay rates having a wavevector dependence of the form $\omega_q = aq^3 + bq + cq^{-1}$ are required to account for these measurements. Previous theoretical work has postulated that the presence of the spectrin network leads to additional terms in the deformation energy of the bilayer. Specifically, the $\omega \sim q$ dependence is explained by an effective surface tension generated by the attachment of the membrane to the underlying spectrin network, while the $\omega \sim q^{-1}$ dependence arises from the uniform confining potential due to this same network (12, 17). The validity of these assumptions and the relation between these additional parameters and the microscale structure of the bilayer/spectrin complex remain somewhat elusive.

The geometry of the RBC membrane can give rise to the observed wavenumber dependence of the undulatory membrane dynamics without requiring the postulate of an effective extra surface tension or a uniform confining potential. In our analysis we simplify the complex shape of a RBC to that of a sphere to produce an analytically tractable model of membrane elasticity and fluid hydrodynamics that still incorporates the effects of the curvature and compact topology of a RBC (18). In the presence of curvature, the bending and compression modes of the membrane become coupled at linear order in the deformation fields. In order to understand the thermally generated height fluctuation spectrum of such a spherical membrane (via the fluctuation-dissipation theorem), we need to account for the full linear response of the membrane to applied (radial) forces; due to the geometric coupling of bending and compression at linear order we are obliged to study both deformation modes. The compression of a flat spectrin network produces a decay rate of the form $\omega_q^{\mathrm{C}} \sim q$ since the restoring force is proportional to q^2 and the hydrodynamic drag acts nonlocally in a manner analogous to that of the undulatory modes. Below, we determine how these modes are mixed in a q-dependent manner by the mean curvature of the membrane so that the height fluctuations incorporate compressional degrees of freedom and thus change their wavenumber dependence. To heuristically argue for the appearance of a regime of $\omega \sim q^{-1}$ behavior, we note that spatially uniform radial displacement of a spherical membrane generates a restoring force associated with both the membrane's change in curvature and area. This response to a uniform radial displacement creates an effectively q-independent restoring force associated previously with a confining potential for the local height fluctuations of the membrane. The combination of this with hydrodynamic drag generates a q^{-1} in the decay rate. We treat both the inner and outer (embedding) fluids as incompressible and the membrane as impermeable so that this effect cannot apply in a uniform manner across the sphere. We rely on more detailed calculations presented below to observe these dynamics at finite wavenumber. From these calculations, we determine the dynamics of these two linearly independent deformation modes of the surface, which are superpositions of bending and compression and couple to the height fluctuations of the membrane. We then calculate the height-height correlation function of the RBC—the experimentally measured quantity. We extract the (visco-)elastic properties of the membrane from these data.

The deformation energy of an elastic shell. The deformation energy of the spherical membrane includes a bending energy F_b and an

in-plane elastic energy F_e. To understand the thermal fluctuations of the membrane, an energy quadratic in the deformations is sufficient. These energies take the well-known Helfrich form (19):

$$F_b = \frac{\kappa}{2}\int d^2s(K_\alpha^\alpha - c_0)^2, \quad [1]$$

$$F_e = \int d^2s\left[\mu E_\alpha^\beta E_\beta^\alpha + \frac{\lambda}{2}(E_\alpha^\alpha)^2\right], \quad [2]$$

where d^2s is an element of area on the surface, $c_0 = 2/R$ is the spontaneous curvature, κ the bending modulus, K_α^β the curvature tensor, λ and μ the two 2D Lamé coefficients required to describe the elasticity of the isotropic composite (i.e. lipid and spectrin) membrane, and E_β^α is a two-dimensional covariant strain tensor. The Greek indices run over the two (angular) coordinates of the undeformed sphere. We expect the bending modulus κ to be dominated by the elastic response of lipid membrane to curvature. The Lamé coefficients in general describe the viscoelastic response of the composite membrane to in-plane deformation. In the frequency domain these are then complex quantities where the imaginary parts reflect the viscous or dissipative response to stress, primarily due to the lipid membrane (of viscosity η_m). Recent membrane diffusion experiments (20) and coarse grained simulations (21) have found an upper bound for the membrane viscosity of 5×10^{-3} μN/m at room temperature. Since the spectrin network's elastic modulus is ∼5 μN/m, the viscous (imaginary) part contribution to the shear response, $-i\omega\eta_m$, is subdominant up to frequencies of $\sim10^3$ Hz. Thus, we fit our data assuming an elastic response to in-plane shear and compression.

The deformation of the membrane can be written as $\epsilon_\alpha = w\hat{r}_\alpha + \mathbf{t}_\alpha$, where w is the radial (i.e. out-of-plane) deformation field, $\hat{r}$ is the unit normal of the sphere, and $\mathbf{t}$ is the in-plane displacement vector. As reviewed in the supplemental materials, the in-plane energy of the sphere contains a term that couples these in-plane and out-of-plane deformations (19). Since the in-plane shear deformations of the membrane do not couple to the out-of-plane deformations, we ignore them throughout this calculation. Therefore, we may write $\mathbf{t}$ as the gradient of a scalar field on the surface of the sphere: $t_\alpha = D_\alpha\Psi$. The free energy of deformation becomes a function of the fields w, Ψ:

$$F_{\rm el}[w,\Psi] = \int d^2s\left\{\frac{\kappa}{2}w\left(\Delta_\perp + \frac{2}{R^2}\right)^2 w + \frac{2K_A}{R^2}w(w+\Delta_\perp\Psi) + \frac{1}{2}(K_A+\mu)(\Delta_\perp\Psi)^2 + \frac{\mu}{R^2}\Psi\Delta_\perp\Psi\right\}, \quad [3]$$

where $\Delta_\perp$ is the two-dimensional Laplacian and $K_A = \mu + \lambda$ is the area compressibility modulus.

Dynamics of a viscoelastic shell in a viscous solvent. To investigate the undulatory dynamics of the membrane, we must consider the coupling of the bulk fluid flows inside and outside the sphere to its deformations. The hydrodynamics can be described by the incompressible Stokes equation (i.e. zero Reynolds number) (18, 22, 23). We allow for a difference between the interior cytosol viscosity η_c and the exterior solvent viscosity η_s. The coupling of the fluid to the membrane is done using stick boundary conditions and the stress balance condition at the surface of the membrane.

Because of the membrane's spherical geometry, the natural basis for the radial w and compression Ψ fields in the overdamped normal modes of the combined fluid/membrane system is the spherical harmonics $Y_{\ell m}(\theta,\psi)$. From rotational symmetry, the normal modes are independent of the azimuthal number m. For each order ℓ, the two normal modes are solutions of the two-by-two matrix equation

$$\begin{pmatrix} w \\ \Psi \end{pmatrix} = \chi(\ell,\omega)\cdot\begin{pmatrix} f_w \\ f_\Psi \end{pmatrix}, \quad [4]$$

where f_w and f_Ψ are the forces acting on the radial and compression fields of the membrane directly. The response matrix χ depends on all the elastic constants of the material, the viscosities of the interior and exterior fluids, the radius of curvature, the order ℓ of the spherical harmonic, and the frequency ω. From the eigenvalues of this matrix we derive the decay rates of each normal mode (23). The decay rates are shown and discussed in more detail in *SI Text*.

The correlation of height fluctuations at two points on the membrane separated by the projected distance d and time t is defined by

$$C(d,t) = \langle w(d,t)w(0,0)\rangle, \quad [5]$$

where the angled brackets denote both spatial and temporal averaging. We measure this correlation function from the experimental fluctuation data using DPM. This correlation function is obtained from the theory outlined above by computing the out-of-plane displacement correlation function between two points on the sphere separated by an angle γ and time difference t in thermal equilibrium. Using the fluctuation-dissipation theorem (FDT) (24), we find that the correlation function in the frequency domain is

$$\tilde{C}(d,\omega) = \left(1-\frac{d^2}{4R^2}\right)\frac{2k_BT}{\omega}\sum_{\ell>0}\mathrm{Im}[\chi_{ww}(\ell,\omega)]P_\ell\left(1-\frac{d^2}{2R^2}\right), \quad [6]$$

where $P_\ell(x)$ is the Legendre polynomial of the ℓth order, R is the radius, $\chi_{ww}(\ell,\omega)$ is the out-of-plane response function, and the distance d between the two points (lying symmetrically about the north pole of the sphere) in question is related to their angular separation γ by $\gamma = 1 - d^2/2R^2$. Since the experiment measures the projection of the radial membrane displacement along the vertical (z) direction, we must rescale the correlation function; the measured correlation function is actually $\tilde{C}(d,\omega) = (1-d^2/4R^2)C(\gamma,\omega)$. The use of the FDT assumes that the observed fluctuations reflect the equilibrium dynamics of the membrane; this is not strictly valid since there are ATP-dependent processes occurring in the membrane that enhance the fluctuations. These processes imply that our extracted moduli are generically smaller than the true ones. To measure this effect, we explore ATP-depleted DCs (DCs −ATP) using our technique.

Results

Using DPM, we measure the height correlations versus the projected distance d at various frequencies ω for the three different morphological groups and for the ATP-depleted DCs (Fig. 3 *A–D* and see *Methods* for detailed procedure). At low frequencies, we observe oscillations in the correlation function at distances of a few microns in the case of the more elastically compliant DC and EC cells. At higher frequencies, these anticorrelations are suppressed, as expected in the more viscously dominated regime.

To extract the moduli, we fit our theory to the measured correlation functions by adjusting the following parameters: the shear μ, the area K_A and bending κ moduli of the membrane, the viscosities of the cytosol η_c and the surrounding solvent η_s, and the radius of the sphere R. We constrain our fits by setting R to the average radius of curvature of the RBC obtained directly from the data. Using a spatially constant curvature is a significant simplifying approximation in the case of DCs. These cells have a stiffer central dimple with highly negative curvature. Thus, we omit membrane fluctuation data from the dimple in our analysis. We also fix the viscosities used to fit all datasets to be $\eta_s =$ 1.2 mPa · s, $\eta_c = 5.5$ mPa · s (25, 26). Based on typical lipid bi-

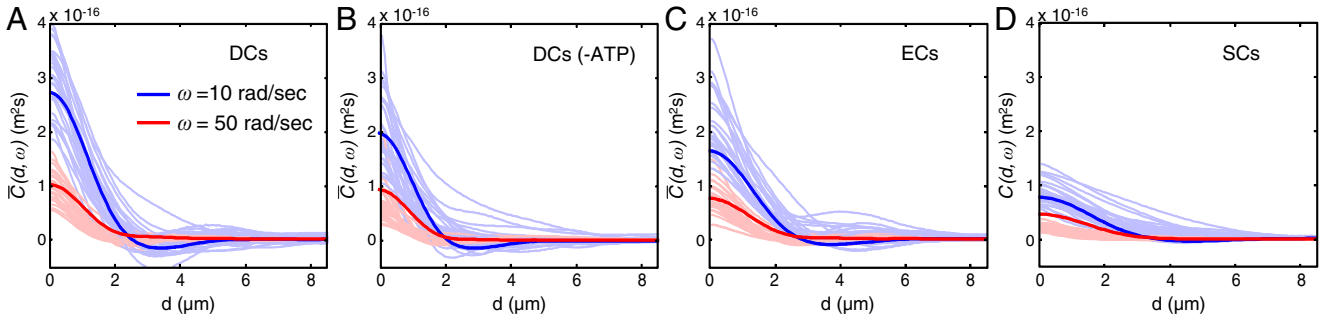

Fig. 3. Height-height correlation function from experiments (faint lines, N = 35 per each group) and calculation (thick lines). (*A*)–(*D*) Height-height correlation function as a projected distance for DCs (*A*), DCs depleted of ATP, ECs (*B*), and SCs (*C*) for $\omega = 10$ rad/sec (blue) and $\omega = 50$ rad/sec (red).

layer viscosities (20, 21) we expect the dissipative part of the membrane elastic constants to be subdominant; this is supported by simultaneous fits of the data at two frequencies a factor of 5 apart with frequency-independent elastic constants. The fitting parameter space is now reduced to three dimensions, spanned by κ, μ, and $K_A = \mu + \lambda$. The shear modulus μ is due to the underlying spectrin network, but the area modulus K_A represents the combined effect of that filament network and the surface tension of the lipid bilayer. As the membrane is tensed in the transition from DCs to SCs due to loss of lipids (discussed further below) we expect the surface tension contribution to λ (and thus to K_A) to increase dramatically. The contribution of the spectrin to λ can be estimated since, for a triangular elastic network $\lambda = \mu$ (27). Any observed increase of λ over μ can thus be attributed to the surface tension of the lipid bilayer.

The experimental data (thin lines) and the best fit of the average data (thick lines) are shown in Fig. 3 *A*–*D*. As can be seen, the theory generates a very good fit to the data including at low frequencies, where anticorrelated motion is observed in DCs and ECs. Both at higher frequencies (red curves) and for stiffer membranes (e.g. SC cells) these anticorrelations are strongly suppressed. The magnitude of the correlation function at short distances is particularly sensitive to the bending modulus κ and its decay over longer distances is principally controlled by the area compression modulus K_A, allowing us to find a unique set of parameters corresponding to the best fits.

The parameters extracted from these fits are shown in Fig. 4 *A*–*D*. Our fit for the bending modulus increases significantly during the DC-EC-SC transition ($p < 10^{-7}$; see *Methods*). Their mean values are 5.6 ± 1.7 (DC), 9.6 ± 3.2 (EC), and 23.9 ± 6.7 (SC) in units of k_BT (Fig. 4*A*). These values are in general agreement with those expected for a phospholipid bilayer $(5–20)k_BT$ (28). In the DCs −ATP we find 6.7 ± 3.3 demonstrating that nonequilibrium processes do not make a statistically significant change to the curvature modulus. Since the bending modulus is presumably controlled by the composition of the lipid bilayer, we hypothesize that its increase implies changes in the lipid composition coincident with the observed morphological transitions. We measured directly the change in surface area of RBCs during the transition from DC to SC morphologies and found a 31% decrease in surface area (not accounting for surface area stored in fluctuations). From this topographical information we find that the surface areas of the three RBC morphologies are, respectively, 139.4 (DC), 143.4 (EC), and 96.3 (SC) in μm^2. This surface area decrease must be accompanied by loss of lipids, via microvesiculation. Previous work indicates that vesiculation changes the lipid chemistry of the RBC. After vesiculation, RBCs have a higher cholesterol/phospholipid ratio and a lower phosphatidylserine/phospholipid ratio compared to the exovesicles shed from the parent RBCs (29). These changes in chemical composition increase the bending modulus of the bilayer as lipids contributing to the lower κ are preferentially shed in the microvesicles; the observed changes in our fitted values of κ are in qualitative agreement with this trend.

The shear modulus results are shown in Fig. 4*B*. They are 7.4 ± 0.9 (DC), 10.4 ± 2.9 (EC), and 12.6 ± 2.1 (SC) in μNm^{-1}. These values are consistent with earlier work based on micropipette aspiration (16), optical tweezers (30), and magnetic twisting cytometry (6). In the latter case we find that, by assuming the ferrimagnetic beads contact the membrane over a $(2.5\ \mu m)^2$

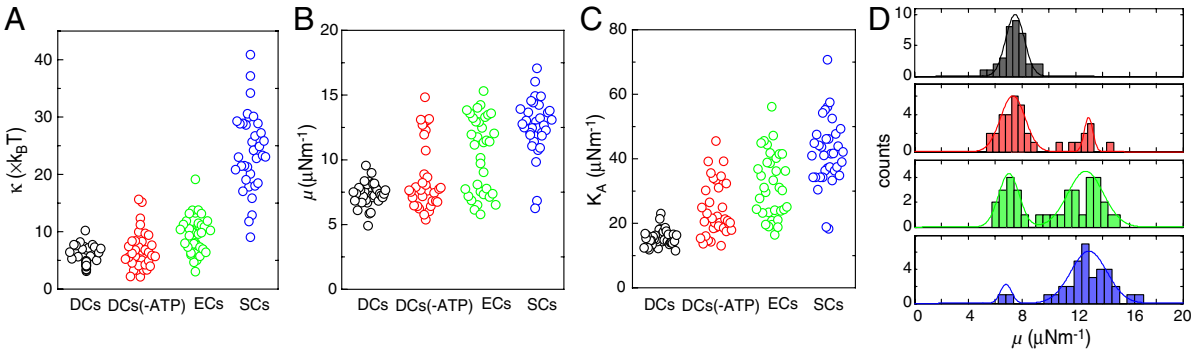

Fig. 4. The bending modulus κ, shear modulus μ, and area modulus $K_A = \mu + \lambda$: (*A*) The membrane bending moduli in units of k_BT of DCs, DCs (−ATP), ECs, and SCs. Their mean values are 5.5 ± 1.7 (DCs), 6.7 ± 3.3 (DCs −ATP), 9.6 ± 3.2 (ECs), and 23.9 ± 6.7 (SCs). The difference in bending moduli between the DCs and DCs −ATP is not statistically significant, but the other differences are, e.g. $p < 10^{-7}$ between both DCs–ECs and ECs–SCs. (*B*) The shear moduli μ of the same cell morphological groups. The *p*-values verify that the differences in the shear moduli between morphological groups are statistically significant: $p < 10^{-5}$ between DCs and ECs, and between DCs and SCs; $p < 10^{-4}$ between ECs and SCs. (*C*) The area moduli $K_A = \mu + \lambda$ for the same groups. (*D*) Distributions of the shear moduli for all four cell types with Gaussian fits are overlapped. The centers of the Gaussian fits are 6.8 (DCs), 6.6 and 13.4 (bimodal: DCs—ATP), 6.1 and 11.7 (bimodal: ECs), and 6.6 and 13.1 (bimodal: SCs) in μNm^{-1}.

patch, our measured shear modulus (for DCs) quantitatively agrees with the results of the twisting technique. In the DCs −ATP we find a bimodal distribution of shear moduli with one group having a value consistent with the DCs (6.6 ± 0.2) and another consistent with the ECs (13.4 ± 0.3). We also observed the overall morphology of the ATP-depleted DCs to transition to the EC form suggesting that the principal effect of ATP depletion is to transform the mean cell shape presumably by altering the coupling of the spectrin to the lipid bilayer. Of those DCs −ATP having the softer shear modulus, we do not observe a statistically significant change from the shear modulus of the ATP-rich DCs suggesting that the nonequilibrium fluctuations do not change these microrheological results at the length and time scales studied. The magnitude of the measured shear modulus of the DCs is also consistent with simple elastic models of the spectrin network. Thus, it appears that the dominant contribution to the in-plane elastic constants of the composite membrane comes from the spectrin. We calculated the shear modulus of a disorder-free triangular network of worm-like chain elastic elements (31). Taking typical values for the lattice constant of the network (90 nm) and persistence length (7.5 nm) (32), we find that the network shear modulus of 5 μNm^{-1} requires a spectrin contour of 197 nm. The previously published value of this quantity is 194 nm (33, 34).

Although there is significant cell-to-cell variation, we find that the mean shear modulus of SCs and ECs is roughly twice that of the DCs ($p < 10^{-5}$)—see Fig. 4*B*. While the histogram of shear moduli of DCs can be fitted by a single Gaussian centered at 6.8 μNm^{-1}, the analogous shear moduli distributions for ECs and SCs are bimodal as shown in Fig. 4*D*. These data suggest that there are essentially two independent conformations of the spectrin network: a soft configuration ($\mu \approx 7$ μNm^{-1}) and a stiff one ($\mu \approx 12$ μNm^{-1}). All DCs have the soft configuration, but the morphological transition to EC and then SC promotes the transition to the stiff network configuration. We speculate that the observed morphological changes are accompanied by modifications of either the spectrin elasticity, the connectivity of the network, or its attachment to the lipid bilayer.

The area modulus results are shown in Fig. 4*C*. They are 15.5 ± 2.5 (DC), 31.7 ± 10.0 (EC), and 41.8 ± 10.3 (SC) in μNm^{-1}. The value for the DCs shows that the contribution of the lipid bilayer surface tension to K_A is small—$\lambda \simeq 1.1\mu$—suggesting a significant reservoir of excess area. For the ECs and SCs lipid surface tension dominates the area modulus—$\lambda > 2\mu$showing that this excess area has been severely reduced under the morphological transition. The area modulus of the DCs −ATP (23.9 ± 8.3 μNm^{-1}) is larger than that of the DCs and statistically consistent with that of the ECs (31.7 ± 10 μNm^{-1}). We attribute this to both a fluctuation enhancement in the DCs due to active processes and to the morphological transition from the DC to the EC form resulting from ATP depletion. Our data cannot resolve these two effects.

Discussion

In summary, we employed diffraction phase microscopy to quantify the undulations of RBC membranes and applied a mathematical model to relate these fluctuations to the mechanical properties of the membrane. We quantified RBC membrane mechanics during the DC-EC-SC cell shape transitions. Our method benefits from a number of advantages over existing microrheological techniques (35). First, DPM is noncontact, providing information on membrane dynamics without the need of probe particles (e.g. beads, cantilevers, etc.) (36). Our technique examines the spatial dependence of the membrane elasticity, which allows for more detailed investigations of the cytoskeleton-bilayer interaction. We found that there is a clear relationship between RBC morphology and elasticity: The normal RBC is most compliant, while the spherocyte is the least. The transition from DCs to SCs is accompanied by a significant loss of lipid resulting in a dramatic increase in the surface tension of the lipid bilayer and in a change of its bending modulus (presumably due to a change in lipid composition during exovesiculation); the area modulus of the DCs, however, is primarily due to the spectrin network as is the shear modulus. Nonequilibrium effects are confined to our measurement of the area modulus as is reasonable since nonthermal fluctuations should alter the area reservoir of the membrane. Since ATP depletion has multiple effects on living cells this role of nonthermal fluctuations is difficult to quantify. A deeper understanding of this relationship between RBC shape and mechanics must incorporate chemical changes in the lipid bilayer and structural changes in the associated spectrin network that occur along with the large-scale morphological changes of the RBC. In addition to its clinical relevance, understanding these coincident morphological/mechanical transitions is fundamental to membrane biology, RBC circulation, and basic studies of cellular mechanics. Further, the RBC is a uniquely suitable model system for studying viscoelastic membrane dynamics, with broad technological implications for encapsulation and drug delivery applications (37).

Methods

Preparation of Red Blood Cells. Blood samples were collected in vacutainer tubes containing Ethylenediaminetetraacetic acid to prevent blood coagulation. The whole blood was centrifuged at 2,000 g at 5 °C for 10 min to separate the RBCs from plasma. The RBCs were then washed three times. The cells were resuspended in an isotonic solution of PBS at a concentration of 10% by volume. Droplets of the suspension were sandwiched between two cover slips and imaged at room temperature. A total of 105 cells were imaged over a period of 4 s, at a rate of 120 images per second: DC (N = 35), EC (N = 35), and SC (N = 35). Our samples were composed of normal, untreated RBCs. However, cells with abnormal morphology formed spontaneously in the suspension (ECs and SCs). RBCs were separated into three groups corresponding to their shapes: DCs, ECs, and SCs. ECs can be classified into three types (type I, II, and III) according to progressive stages in formation and maturation (38, 39). We have excluded type III ECs (with high speculation) and have analyzed only type I and II ECs. For DCs −ATP group, the cytoplasmic pool of ATP was depleted by incubating the DCs without glucose, in the presence of 5 mM inosine (A3221, Sigma-Aldrich) and 3 mM iodoacetamide (I1024, Sigma-Aldrich) for 2 h at 20 °C. On rare occasions, some cells do not sit flat on the glass substrate, which is apparent from the profile of the phase image. In order to avoid complications, we removed these cells from the batch. The shape effects, i.e. tangential components of the fluctuations, were neglected in our analysis, which is justified because they significantly affect only the low-q region of our measurements.

Quantitative Phase Imaging of RBCs. We employed diffraction phase microscopy (DPM) to obtain high-speed quantitative phase images of RBCs. DPM employs the principle of laser interferometry in a common path geometry and thus provides full-field quantitative phase images of RBCs with 0.2 nm optical path-length stability (15). The instantaneous cell thickness map was obtained as $h(x, y, t) = (\lambda/2\pi\Delta n)\phi(x, y, t)$, with $\lambda = 514$ nm the wavelength of the laser light used, $\Delta n = 0.06$ the refractive index contrast between the RBC and the surrounding PBS (38), and ϕ the quantitative phase image measured by DPM. The DPM optical path-length stability corresponds to a membrane displacement of 3.3 nm, which is the lower limit of our measurable range, without using spatial or temporal averaging. An Ar^{++} laser (514 nm wavelength) was used as the illumination source for an Olympus IX71 inverted microscope. The microscope was equipped with a 40× objective (0.65 NA), which grants a diffraction-limited transverse resolution of 400 nm. With the additional relay optics used outside the microscope, the overall magnification of the system was approximately 200. The interferograms are captured by an electron multiplying CCD camera (PhotonMAX 512B, Princeton Instruments, Inc.).

Membrane Displacement Analysis The instantaneous cell displacement map $\Delta h(x, y, t)$ was obtained by subtracting the time-averaged cell shape from each thickness map in the series. We defined mean squared displacement map as time-averaging of squared displacement map. For the height-height correlation function $\tilde{C}(d, \omega)$, we first applied the Fourier transform spatially and temporally to convert the cell displacement map $\Delta h(x, y, t)$ into $\Delta h(q_x, q_y, \omega)$, where q_x, q_y are the components of the wavevector in the plane of the membrane. The spatial correlation function was obtained as

$\bar{C}(d,\omega) = \int |\Delta h(q_x, q_y, \omega)|^2 \exp[i(q_x x + q_y y)] d^2\mathbf{q}$. The correlation functions, $\bar{C}(d,\omega)$, shown in Fig. 3 *A–C* were calculated assuming azimuthal symmetry and using $d = \sqrt{x^2 + y^2}$. The very outer rims of all RBCs and the central "dimple" of the DCs were masked out and thus excluded from the analysis.

Simplified Geometric Model of the RBC. Accounting for the role of the RBC's curvature is necessary to understand the observed membrane dynamics, but the approximation of each cell by a sphere requires justification. While this is a reasonable approximation of the global geometry of a SC, the EC is better approximated as an oblate ellipsoid. The DCs can also be approximated in the same way if one excludes the central "dimple." In the latter two cases, we approximate the global shape of the cells as best-fit spheres having a radius R_{eff} determined by the mean radius of curvature of the cell. For the discocytes we mask out the fluctuation data from a circular domain of radius 1.3 μm centered around the dimple so as to not include membrane fluctuations from regions having local curvatures greatly different from the mean. We compute this best-fit or effective radius as follows: Assume that the radius of an RBC's projection on imaging (*xy*) plane is *r* and its average height above that plane is *h*; denote $t = R_{\text{eff}} - h$. From geometry, we have $t^2 + r^2 = R_{\text{eff}}^2$. Thus, we can calculate the effective radius R_{eff} using $R_{\text{eff}} = (r^2 + h^2)/2h$. From this we calculate from the cell images the following values for the effective radii: $R_{\text{eff}}(\text{DC}) = 7.22 \pm 0.25$ μm, $R_{\text{eff}}(\text{EC}) = 10.09 \pm 0.7$ μm, and $R_{\text{eff}}(\text{SC}) = 5.54 \pm 0.7$ μm.

RBCs have spatial variations of their local mean curvature, which we ignore. We justify this approximation by noting that the data analysis averages the fluctuation measurements over the entire cell surface, so these local curvature variations are averaged over in the analysis. Secondly, even in the cell morphology, having the most spatial variation in local curvature (DC), the effective radius of curvature extracted from our fitting procedure outlined above is very close to the mode (i.e. most common) local radius of curvature on the cell. Thus, the effective radius of curvature used reflects the typical values on the surface. To demonstrate this point we examined the spatial heterogeneity of local mean curvatures by calculating the local radius of curvature in 240 nm × 240 nm patches over the visible cell surface of a DC. The peak of the distribution is near to $1/R_{\text{eff}}(\text{DC}) = 0.138$ μm^{-1}. The region of negative curvature, the central "dimple" was excluded from our analysis.

Curve fitting for height-height correlation was carried out using MatLab software and a custom built code by minimizing the mean square error. All data were fitted in a batch procedure, with an identical limit and step for each parameter. *p*-values are calculated by two-tailed Mann-Whitney rank sum tests comparing bending modulus values between different groups. All the numbers that follow the ±sign in the text are standard deviations.

ACKNOWLEDGMENTS. A.J.L. thanks W. Gelbart for enjoyable conversations. This research was supported by the National Institutes of Health (P41-RR02594-18). Y.P. was supported by Cambridge Foundation Fellowship, Whitaker Health Sciences Fellowship, and Samsung Scholarship. G.P. was partially supported by the National Science Foundation (08-46660 CAREER). A.J.L. acknowledges partial support from NSF-DMR-0907212.

1. Brochard F, Lennon JF (1975) Frequency spectrum of the flicker phenomenon in erythrocytes. *J Phys-Paris* 36:1035–1047.
2. Bao G, Suresh S (2003) Cell and molecular mechanics of biological materials. *Nat Mater* 2:715–725.
3. Fournier JB, Lacoste D, Raphael E (2004) Fluctuation spectrum of fluid membranes coupled to an elastic meshwork: Jump of the effective surface tension at the mesh size. *Phys Rev Lett* 92:018102.
4. Discher DE, Mohandas N, Evans EA (1994) Molecular maps of red cell deformation: Hidden elasticity and in situ connectivity. *Science* 266:1032–1035.
5. Engelhardt H, Gaub H, Sackmann E (1984) Viscoelastic properties of erythrocyte membranes in high-frequency electric fields. *Nature* 307:378–380.
6. Puig-de-Morales-Marinkovic M, Turner KT, Butler JP, Fredberg JJ, Suresh S (2007) Viscoelasticity of the human red blood cell. *Am J Physiol-Cell Ph* 293:C597–605; Marinkovic M, et al. (2009) Febrile temperature leads to significant stiffening of Plasmodium falciparum parasitized erythrocytes. *Am J Physiol-Cell Ph* 296:C59–64.
7. Browicz T (1890) Further observation of motion phenomena on red blood cells in pathological states. *Zbl med Wissen* 28:625–627.
8. Zilker A, Ziegler M, Sackmann E (1992) Spectral analysis of erythrocyte flickering in the 0.3–4 μm^{-1} regime by microinterferometry combined with fast image processing. *Phys Rev A* 46:7998–8001.
9. Tuvia S, Levin S, Bitler A, Korenstein R (1998) Mechanical fluctuations of the membrane-skeleton are dependent on F-actin ATPase in human erythrocytes. *J Cell Biol* 141:1551–1561.
10. Kaizuka Y, Groves J (2006) Hydrodynamic damping of membrane thermal fluctuations near surfaces imaged by fluorescence interference microscopy. *Phys Rev Lett* 96(11): 118101.
11. Popescu G, et al. (2005) Erythrocyte structure and dynamics quantified by Hilbert phase microscopy. *J Biomed Opt* 10:060503.
12. Popescu G, et al. (2006) Optical Measurement of Cell Membrane Tension. *Phys Rev Lett* 97:218101.
13. Popescu G, Badizadegan K, Dasari R, Feld M (2006) Observation of dynamic subdomains in red blood cells. *J Biomed Opt* 11:040503.
14. Popescu G, Ikeda T, Dasari RR, Feld MS (2006) Diffraction phase microscopy for quantifying cell structure and dynamics. *Opt Lett* 31:775–777.
15. Park YK, Popescu G, Badizadegan K, Dasari RR, Feld MS (2006) Diffraction phase and fluorescence microscopy. *Opt Express* 14:8263–8268.
16. Waugh R, Evans EA (1979) Thermoelasticity of red blood cell membrane. *Biophys J* 26:115–131.
17. Gov N, Zilman AG, Safran S (2003) Cytoskeleton confinement and tension of red blood cell membranes. *Phys Rev Lett* 90:228101.
18. Seifert U (1997) Configurations of fluid membranes and vesicles. *Adv Phys* 46:13–137.
19. Zhang Z, Davis HT, Kroll DM (1993) Scaling behavior of self-avoiding tethered vesicles. *Phys Rev E* 48:R651–654.
20. Cicuta P, Keller SL, Veatch SL (2007) Diffusion of liquid domains in lipid bilayer membranes. *J Phys Chem B* 111:3328–3331.
21. den Otter WK, Shkulipa SA (2007) Intermonolayer friction and surface shear viscosity of lipid bilayer membranes. *Biophys J* 93:423–433.
22. Rochal SB, Lorman VL, Mennessier G (2005) Viscoelastic dynamics of spherical composite vesicles. *Phys Rev E* 71:021905.
23. Kuriabova T, Levine AJ (2008) Nanorheology of viscoelastic shells: Applications to viral capsids. *Phys Rev E* 77:031921.
24. Chaikin PM, Lubensky TC (1995) *Principles of Condensed Matter Physics* (Cambridge Univ Press, New York).
25. Hochmuth RM, Buxbaum KL, Evans EA (1980) Temperature dependence of the viscoelastic recovery of red cell membrane. *Biophys J* 29:177–182.
26. Kelemen C, Chien S, Artmann GM (2001) Temperature transition of human hemoglobin at body temperature: Effects of calcium. *Biophys J* 80:2622–2630.
27. Feng S, Sen PN (1984) Percolation on elastic networks: New exponent and threshold. *Phys Rev B* 52:216–219.
28. Hubbard AT (2002) *Encyclopedia of Surface and Colloid Science* (Marcel Dekker, New York).
29. Hagerstrand H, Isomaa B (1994) Lipid and protein composition of exovesicles released from human erythrocytes following treatment with amphiphiles. *Biochim Biophys Acta* 1190:409–415.
30. Dao M, Lim CT, Suresh S (2003) Mechanics of the human red blood cell deformed by optical tweezers. *J Mech Phys Solids* 51:2259–2280.
31. Tang W, Thorpe MF (1988) Percolation of elastic networks under tension. *Phys Rev B* 37:5539.
32. Li J, Dao M, Lim CT, Suresh S (2005) Spectrin-level modeling of the cytoskeleton and optical tweezers stretching of the erythrocyte. *Biophys J* 88:3707–3719.
33. Siegel D (1985) Partial purification and characterization of an actin-bundling protein, band 4.9, from human erythrocytes. *J Cell Biol* 100:775–785.
34. Marko JF, Siggia ED (1995) Stretching DNA. *Macromolecules* 28:8759–8770.
35. Waigh TA (2005) Microrheology of complex fluids. *Rep Prog Phys* 68:685–742.
36. Bursac P, et al. (2005) Cytoskeletal remodelling and slow dynamics in the living cell. *Nat Mater* 4:557–561.
37. Walker SA, Kennedy MT, Zasadzinski JA (1997) Encapsulation of bilayer vesicles by self-assembly. *Nature* 387:61–64.
38. Park Y, et al. (2008) Refractive index maps and membrane dynamics of human red blood cells parasitized by Plasmodium falciparum. *Proc Natl Acad Sci USA* 105:13730–13735.
39. Bessis M, et al. (1977) *Blood Smears Reinterpreted* (Springer, New York).